# In-depth study of the formation processes of single atmospheric particles in the southeastern margin of Tibetan Plateau

Li Li[1,3], Qiyuan Wang[1,2], Jie Tian[1], Huikun Liu[1], Yong Zhang[1], Steven Sai Hang Ho[4], Weikang Ran[1], Junji Cao[5]

[1] Key Laboratory of Aerosol Chemistry and Physics, State Key Laboratory of Loess and Quaternary Geology, Institute of Earth Environment, Chinese Academy of Sciences, Xi'an 710061, China
[2] CAS Center for Excellence in Quaternary Science and Global Change, Xi'an 710061, China
[3] University of Chinese Academy of Sciences, Beijing 100049, China
[4] Division of Atmospheric Sciences, Desert Research Institute, Reno, NV 89512, United States
[5] Institute of Atmospheric Physics, Chinese Academy of Sciences, Beijing 100029, China

Correspondence to: Qiyuan Wang (wangqy@ieecas.cn) and Junji Cao (jjcao@mail.iap.ac.cn).

**Abstract**

The unique geographical location of the Tibetan Plateau (TP) plays an important role in regulating global climate change, but the impacts of the chemical components and atmospheric processing on the size distribution and mixing state of individual particles are rarely explored in the southeastern margin of the TP, which is a transport channel for pollutants from Southeast Asia to the TP during the pre-monsoon season. Thus a single-particle aerosol mass spectrometer (SPAMS) was deployed to investigate how the local emissions of chemical composition interact with the transporting particles and assess the mixing state of different particle types and secondary formation in this study. The TP particles were classified into six distinct types, mainly including the largest fraction of the rich-potassium (rich-K) type in the total particles (30.9%), followed by the biomass burning (BB) type (18.7%). Most particle types were mainly transported from surroundings the sampling site and along the Sino-Myanmar border; but the air mass trajectories from northeastern India and Myanmar show a greater impact on the number fraction of BB (31.7%) and Dust (18.2%) types, respectively. Then, the two episodes with high particle concentrations showed that the differences in the meteorological conditions in the same trajectory clusters could cause significant changes in chemical components, especially the Dust and EC-aged types, which changed by a sum of 93.6% and 72.0%, respectively. Ammonium and Dust particles distribute at a relatively larger size (~ 600 nm), but the size peak of other types is present at ~ 440 nm. Compared with the abundant sulfate ($^{97}HSO_4^-$), the low nitrate ($^{62}NO_3^-$) internally mixed in TP particles is mainly due to the fact that nitrate is more volatilized during the transport process. The formation mechanism of secondary speciation demonstrate that the formation capacity of atmospheric oxidation is presumably affected by the convective transmission and the regional transport in TP. However, the relative humidity (RH) could significantly promote the formation of secondary species, especially $^{97}HSO_4^-$ and $^{18}NH_4^+$. This study provides new insights into the particle composition and size, mixing state, and aging mechanism in high time resolution over the TP region.

**Keywords**

Southeastern Tibetan Plateau, Individual particles, Chemical characteristics, mixing state,

Secondary formation

## 1 Introduction

Atmospheric aerosols have complex components and sources and can be coated with inorganic or organic materials during transport and atmospheric processing (Crippa et al., 2013), and then its sizes, chemical compositions, mixing states and optical properties would change greatly, leading to its influence in the atmosphere more uncertain (Jacobson, 2002; Zaveri et al., 2010; Matsui, 2016; Budisulistiorini et al., 2017; Ma et al., 2012). Currently, the influences of the complex chemical components on aerosol size and mixing state show large regional differences due to the variations in the pollution sources, atmospheric formation mechanism and meteorological conditions, which have been widely studied in an urban area at a low altitude (Pratt et al., 2011; Liu et al., 2020a; Xu et al., 2017; Wang et al., 2022). However, Liu et al (2020) have found that the migration or formation of low-volatile component (such as nitrate and organic matter) could effectively be reduced due to evaporation during the upward transportation process, which further alter the chemical compositions and the particle sizes. The transportation of the aerosols to a relatively cleaner environment prevails the formation of secondary chemicals at a high altitude (Liu et al., 2020b). Therefore, a comprehensive investigation of the detailed characteristic of aerosol formation and mixing states is required to understand their environmental effects in low-, and high-altitude.

As a typical high-altitude region, the Tibetan Plateau (TP) has the highest and largest mountain area in the world, which is the most sensitive and obvious indicator of climate change in the entire Asian continent (Liu et al., 2017; Chen and Bordoni, 2014; Immerzeel et al., 2010). Numerous studies have shown that the melting and retreat of glaciers in the TP regions is accelerating in recent decades, largely attributed to anthropogenic emissions, such as greenhouse gases and aerosols (Luo et al., 2020; Hua et al., 2019). Atmospheric aerosols also can act as cloud condensation nuclei to impact the local hydrological cycles and monsoon patterns by changing the microphysical properties and life span of clouds (Qian et al., 2011; Gettelman et al., 2013; Kumar et al., 2017). The southern part of the TP is always affected by the transport of more polluted air from South Asia along the mountain valleys,

especially during the pre-monsoon (i.e., March-May) with the southwest prevailing wind (Chan et al., 2017; Zhao et al., 2017; Han et al., 2020). Most studies have focused on the optical characteristics within the TP; however, only a few research has been conducted on aerosol components.

Present researches on aerosol components over the TP mostly focus on exploring the influence of light-absorbing carbon aerosols and dust particles on climate change by optical or offline sampling methods (e.g., Wang et al., 2019a; Liu et al., 2021). There is a lack of studies on the chemical composition, mixing states, and formation mechanism of aerosols in the southeast margin and even the entire TP, especially using high-time resolved measurements. Although time-integrated sampling with filter collection followed by laboratory analyses has been widely adopted for the chemical characterization of aerosols (Li et al., 2022a; Shen et al., 2015; Zhang et al., 2013), the drawbacks of the traditional approach need to get attention, including the low time resolution, high detection limit, and time- and labor-intensive procedures. Therefore, more advanced aerosol measurement equipment with high-time resolution are developed, for example the aerosol chemical speciation monitor (ACSM) and aerosol mass spectrometer (AMS) (Ng et al., 2011; Canagaratna et al., 2007) are mainly achieved the online observation datasets of non-refractory submicron aerosol (including the mass concentration of sulfate, nitrate, ammonium, chloride and organic; and mass spectral of organic). This is beneficial to recognize the dynamic processes of source emission of organic matter in the atmosphere (Du et al., 2015; Zhang et al., 2019a). Meanwhile, aerosol time-of-flight mass spectrometry (ATOFMS) (Dall'Osto et al., 2014) and single particle aerosol mass spectrometer (SPAMS) (Zhang et al., 2020) are popular for characterizing atmospheric individual particles. These devices can determine the chemical composition and size distribution of the particles in detail, such as the dynamic processes of chemical aging, mixing state and transporting (Liang et al., 2022; Li et al., 2022b; Zhang et al., 2019b). To the best knowledge, the advanced measurement device has not yet been applied for the studies conducted in TP, leading to a lack of in-depth research on the $PM_{2.5}$ pollution in TP, especially in the southeastern margin, which hinders our understanding of the distribution characteristics and formation mechanism of aerosol components in high-altitude regions.

The southeastern margin of the TP is an important transitional zone between the high-altitude TP and the low-altitude Yungui Plateau (Wang et al., 2019a; Zhao et al., 2017), is an ideal place for investigating the impacts of pollutants transport and formation in the high-altitude zone. In this study, continuous field observation of individual particles (SPAMS) was deployed on the southeastern margin of the TP during the pre-monsoon period, to (i) investigate the changes of chemical characteristics between transport and local fine particles during pre-monsoon, (ii) determine the size distributions and mixing states of different particle types, and (iii) assess the contributions of photooxidation and aqueous reaction to the formation of the secondary species. These results would expand our understanding of the chemical components, size distribution, mixing state and aging pathways of aerosols in the high-altitude areas over the TP and surrounding areas.

## 2 Methodology

### 2.1 Sampling site

Intensive one-month field observation was deployed at the rooftop (~ 10 m above ground level) of the Lijiang Astronomical Station, Chinese Academy of Sciences (3260 m above sea level; 26°41′24″N, 100°10′48″E), Gaomeigu County, Yunnan Province, China, during the pre-monsoon period (from April 14$^{th}$ to May 13$^{th}$, 2018). The nearest residential area is the Gaomeigu village (3–5 km away) with a small population size of 113 residents in 27 households. Villagers earn a living by farming (e.g., potato and autumn rape), and biomass is the major domestic fuel (Li et al., 2016). The sampling site is surrounded by rural and mountainous areas and has no obvious industry or traffic emissions. During the total observation period, the average temperature (T) and relative humidity (RH) are 8.4 ± 3.1℃ and 69% ± 21%, respectively. The wind speed (WS) is 2.2 ± 1.2 m·s$^{-1}$ with the prevailing wind in the north and northeastern (Fig. S1).

### 2.2 On-line instrument

A detailed operational principle and the calibrations of the single-particle aerosol mass spectrometer (SPAMS, Hexin Analytical Instrument Co., Ltd., Guangzhou, China) has been described elsewhere (Li et al., 2011). Briefly, individual particles are drawn into SPAMS

through a critical orifice. The particles are focused and accelerated, then aerodynamically sized by two continuous diode Nd: YAG laser beams (532 nm), subsequently desorbed and ionized by a pulsed laser (266 nm) triggered exactly based on the velocity of the specific particle. The generated of positive and negative molecular fragments are recorded with the corresponding size of individual particles. In summary, a velocity, a detection time, and an ion mass spectrum are recorded for each ionized particle, while there is no mass spectrum for not ionized particles. The velocity could be converted to $d_{va}$ based on a calibration using polystyrene latex spheres (PSL, Thermo Scientific Corp., Palo Alto, USA) with predefined sizes. The average ambient pressure is 690 hPa (in a range of 685–694 hPa) during the measurements and calibration. Particles measured by SPAMS mostly are within the size range of vacuum aerodynamic diameter ($d_{va}$) 0.2–2.0 μm. A hollow silicone dryer was installed in front of the inlet. This reduces the uncertainty of particle collection efficiency due to the changes of humidity in sampled airs.

Meteorological parameters, including the temperature (℃), RH (%), WS ($m \cdot s^{-1}$), and wind direction (WD) were continuously achieved using an automatic weather station (Model MAWS201, Vaisala HydroMet, Helsinki, Finland) in a 5-min resolution, and the planetary boundary layer (PBL) was acquired from the website (https://rda.ucar.edu/datasets/ds083.2, last access: 17 April 2020) in a 1-hour resolution. Gaseous concentrations (ppbv) were obtained using a multiple gas analyzer (Thermo Scientific Corp.), including ozone ($O_3$, model 49i) and nitrogen oxides ($NO_x$, model 42i) in a 5-min resolution. The SPAMS and gas analyzers are co-located in the same position, and the weather station was uncovered outside ~5 m from the sampling house. Time series of SPAMS particles, gaseous concentrations (NO, $NO_x$, $O_3$, and CO) and meteorological parameters (PBL, temperature, RH, WD, and WS) were shown in Fig. S2.

### 2.3 Individual particle classification

During the observation period, a total of 461,876 ambient particles with the size ($d_{va}$) of 0.2–2.0 μm were collected, including 55,583 in Episode 1 (E1; from April 18$^{th}$ 08:00 local time (LT) to April 19$^{th}$ 08:00 LT) and 62,110 in Episode 2 (E2; from April 26$^{th}$ 17:00 LT to April 28$^{th}$ 02:00 LT). The analyzed particles are classified into 1,557 groups using an adaptive

resonance theory neural network (ART-2a) with a vigilance factor of 0.8, a learning rate of 0.05, and 20 iterations (Song et al., 1999). Finally, eight major particle clusters [i.e., potassium-rich (rich-K), biomass burning (BB), organic carbon (OC), Ammonium, aged element carbon (EC-aged), Dust, sodium (Na)-potassium (K)-containing (NaK-SN), and iron (Fe)-lead (Pb)-containing (Metal)] with distinct chemical patterns were manually combined, which represent ~99.7 % of the population of the detected particles. The remaining particles are grouped as "Other". The characteristics of the positive and negative mass spectra (MS) of each particle type are shown in Fig. S3. A detailed description of classification criteria for individual particles and the characteristic ion fragments for each particle type can be found in Text S1. The criteria used for searching the some secondary species in the SPAMS datasets are summarized in Table S2.

### 2.4 Trajectory-related analysis

To determine the influence of regional transport on different particles at the southeastern margin of the TP, the trajectory clusters analysis was carried out using the 72-h backward air mass trajectories at arrival heights of 500 m above ground level. The trajectories were calculated with the Hybrid Single-Particle Lagrangian Integrated Trajectory model (Draxler and Hess, 1998), and the meteorological data were obtained from the Global Data Assimilation System (GDAS; ftp://arlftp.arlhq.noaa.gov/pub/archives/gdas1, last access: 6 April, 2022). The cluster analysis employs a Euclidean-oriented distance definition to differentiate and cluster the major spatial features of the inputting trajectories. Details of the trajectory clustering method can be found in Sirois and Bottenheim (1995). To investigate the effects of transport on the chemical characteristic of the individual particles, trajectories with particle number concentrations high than the 75$^{th}$ percentile are considered as pollution (Liu et al., 2021).

## 3 Results and Discussion

### 3.1 Characteristics of particle composition

Table 1 summarizes the numbers of concentrations, relative percentages and characteristic ions of each particle type. The most dominant particle type in Gaomeigu during

pre-monsoon is rich-K, accounting for an average of 30.9% of the total resolved particles, followed by BB (18.7%), OC (12.8%), Ammonium (11.9%), EC-aged (10.9%) and Dust (10.7%). Their characteristics of mass spectrum and possible sources are described in supplemental information of text S1 in detail. Similar to the results of some studies in urban areas, rich-K or carbonaceous-containing type is the dominant particle type (15-50%) (Xu et al., 2018; Wang et al., 2019b; Li et al., 2022). Combined with the previous studies and the characteristics of the mass spectrum (Fig. S3a) in this study, the rich-K particles are contributed by biomass burning and traffic emission, because that extensive works usually identify abundant $^{39}K^{+}$ signals for biomass burning (Pratt et al., 2011; Chen et al., 2017), while the presence of phosphate (*m/z* $^{79}PO_3^{-}$) indicates the vehicle exhaust (Yang et al., 2017). The results of the correlation between seven variables (Fig. S4) show that rich-K type was strongly correlated with Ammonium (r=0.84) and EC-aged (r=0.90) types, follow well correlated with OC (r=0.70) and BB (r=0.68) types, further demonstrate that rich-K particles type is from traffic emission and biomass burning, and is affected by secondary formation during the atmospheric aging in southeastern TP. It is worth noting that few research have captured the high proportion of Ammonium particles as shown in this study (Shen et al., 2017; Xu et al., 2018), which is ascribed to the conversion of ammonia ($NH_3$) precursor emitted from large-scale agricultural activities and mountain forest (Engling et al., 2011; Li et al., 2013). It is necessary to point out that 60% of Ammonium particles contain signals of amine fragment (*m/z* 58, $C_2H_5NH{=}CH_2^{+}$), implying their similar formation pathway (Zhang et al., 2012). Moreover, the amine-containing particle represented 12.5% of the total ambient particles, which is significantly higher than that in some urban areas at low altitudes (around 2%) (Cahi et al., 2012; Zhang et al., 2015; Li et al., 2017) but is comparable to that at observed sites with high RH, or during fog and cloud events at a high altitude (> 9%) (Roth et al., 2016; Lin et al., 2019). This suggests that the formation of amines under high RH and fog conditions might exist in the Gaomeigu area (with an altitude of 3260 m), for example, the high relative fraction of amine-containing particle corresponds to a high RH (Fig. S5), and the existence of amine sources govern the ammonium formations (Bi et al., 2016; Rehbein et al., 2011). The relatively larger fraction of Dust particles is related to the short-time occurrences of dust events in spring (Fig. S6), leading to a wide contribution ranging between

10% and 70% in the period of 19:00 LT on April 16$^{th}$ to 10:00 LT on April 17$^{th}$.

Fig. 1 shows the diurnal variations of each particle type. The rich-K, BB and OC particles decrease after midnight until 06:00 LT, possibly explained by the curtailment of local traffic and biomass-burning activities at nighttime even though both the planetary boundary layer (PBL) height and WS decrease (Fig. S7). Then, their concentrations rapidly increase in the morning (around 07:00 LT) due to more pollutants from biomass burning and traffic emissions at the upwind region. The increases of PBL height and WS also lead to the transported of air pollutants from the surrounding regions to the sampling site (Liu et al., 2021). At 11:00 LT, the particle concentrations sharply decrease till 16:00–17:00 LT, caused by the pollutant dispersion with the continuing increases of the PBL height and WS. Increasing trends are observed after 17:00 LT due to the pollutant accumulation with the reduction of PBL height and WS. In contrast, the Ammonium, EC-aged and Dust particles show a unimodal pattern of the daily diurnal variation (Fig. 1d–f). From 00:00 to 06:00 LT, minor fluctuation of particle concentrations of Ammonium, EC-aged and Dust is observed for these particle types. After that, their levels continuously elevate until ~11:00 LT due to the regional transport, traffic emission and fugitive dust (Text S2). While the PBL height and WS increase continuously, the Ammonium, EC-aged and Dust types begin to decline from 12:00 to 17:00 LT. The subsequent increases of these three types after 17:00 LT are attributed to the reduction of PBL height, as a result of the accumulation of pollutants in the near-surface atmosphere.

Based on the transport pathways, four air mass clusters are identified to investigate the effect of regional transport on the major particle types (i.e., rich-K, BB, OC, Ammonium, EC-aged and Dust) (Fig. 2). Cluster 1, 3 and 4 are originated from northeastern Myanmar, accounting for 59.8%, 33.2% and 4.6% of the total trajectories, respectively. Cluster 1 had an average percentage of 32.7%, 18.5%, 12.0%, 12.5%, 11.1% and 8.9%, respectively, on the rich-K, BB, OC, Ammonium, EC-aged and Dust particles (Table S1). Cluster 3 and 4 have the comparable contributions of OC (15.5% and 12.5%, *respectively*), increased of BB (19.3% and 26.8%, *respectively*) and decreased of rich-K (26.8% and 25.2%, *respectively*), Ammonium (10.4% and 7.7%, *respectively*) and EC-aged (7.7% and 6.3%, *respectively*), to

those of Cluster 1, but with a high contribution of Dust (16.6%), which refer Cluster 3 and 4 to as dust and biomass burning pollution. However, Cluster 1 is more influenced by compound pollution, mainly including secondary formation, biomass burning, and traffic emissions. The diurnal variations of the BB and OC fractions are similar which rapidly elevate at 07:00 LT (Fig. S8) due to the increased contribution of biomass burning and traffic emissions from Cluster 1, Ammonium and EC-aged particles (peak at 07:00 LT) caused by the effect of Cluster 1 and 3 together. A stable diurnal variation of rich-K fraction is mainly due to its large proportion and diverse sources. The similar diurnal trend of Clusters 3 and 4 are both associated with dust contributions, which decrease at 04:00 LT and increase at noon. The increased nighttime particles could be attributed to the pollutant accumulation with the decreased PBL height. Cluster 2 originate from the northeastern India and passes over Bangladesh. This cluster accounts for only 2.4 % of the total trajectories, in which ~30.8% and ~35.9% are mainly associated with the rich-K and BB particles, respectively. Although Cluster 2 and 4 are composed of a small fraction of total trajectories (2.4% and 4.6 %, respectively), BB and dust particles are identified as the major pollutants, suggesting significant influences from India and northeastern Myanmar during the campaign.

A more in-depth investigation of the characteristics of the main particle types in the southeastern Tibet Plateau was conducted during two episode periods when the number concentration of particles was high (i.e., E1: from 08:00 LT April 18$^{th}$ to 08:00 LT April 19$^{th}$, 2018; E2: 17:00 LT April 26$^{th}$ to 02:00 LT April 28$^{th}$, 2018) (Fig. S6). Even though the two episodes are contributed by Cluster 1, the chemical components show significant differences (Table 1). During E1, the average fractions of the rich-K, BB, OC, Ammonium, EC-aged, and Dust particle are 29.0%, 11.5%, 8.1%, 17.5%, 10.0% and 20.3%, respectively, different from 39.3%, 14.2%, 10.0%, 13.5%, 17.2%, and 1.3% respectively, during E2. It can be seen that the major changed factor of the Dust particle is 93.6% lower during E2 than E1, whereas the EC-aged particle shows a reversible of 72.0% higher during E2. Meanwhile, rich-K, BB and OC particles also increase by 35.5%, 23.5% and 23.4% respectively during E1 compared to E2. For the air mass clusters (Fig. S9), E1 and E2 exhibit minor differences, mostly originating from northern Myanmar and the Sino-Burmese border, but not identical regions.

The Dust particles that are much lower during E2 than E1 could be explained by higher WS (on average of 2.7 ± 1.0 m/s versus 0.4 ± 0.5 m/s) (Fig. S9) and PBL height (771 ± 717 m versus 560 ± 549 m) (Fig. S10). The Dust particles are mainly formed by re-suspension in the local areas. In addition, the quick thrown-up dust belongs to more coarse size particles, which are out of the detection range of the SPAMS. However, due to the larger dust particles deposited more easily under the low WS and the stagnant air conditions during E1, more suspended dust particles of small size fall in the detection range of SPAMS. Moreover, the increased PBL height and WS could speed up the transportation of pollutants from multiple sources (e.g., traffic and biomass burning emissions) to the observation site, leading to elevate the fraction of EC-aged, rich-K, BB, and OC particles during E2. The decreased Ammonium fraction during E2 is potentially explained by the reductions in the secondary pollutant formation with declines of RH (from 73.9% ± 23.9% to 53.1% ± 14.9%), in comparison to those during E1.

### 3.2 Characteristics of size distribution and mixing state

The aerodynamic size distributions of all particle types are shown in Fig. 3. According to the characteristics of the average MS (Text S1 and Fig. S3), rich-K, BB, OC and EC-aged particles originated from the similar sources of solid-fuel combustion or vehicle emission Their size distribution thus presents within a small-scale (~440 nm) (Fig. S11a). However, the relative percentage of each particle type is distinct with different size ranges, possibly due to the unique atmospheric processing. For example, as shown in Fig. 3a, the proportions of rich-K and BB types increases along with the increase in particle size from 200 to 420 nm, then decrease. OC and EC-aged types are mainly distributed in relatively small sizes, and their proportions gradually decrease when the size ranges become lager. Ammonium and Dust types are mainly distributed in large sizes of ~600 nm (Fig. S11a). The proportion of Ammonium particles gradually increases with the increase of particle size and peaks at 740 nm, the relatively large size distribution is ascribed to the intense atmospheric aging during regional transport (Text S1). The proportion of Dust particles gradually increases with a size > 560 nm and peaks at 1.48 μm. This is consistent with the fact that dust is a coarse particle, generally formed at the roadside and fly ash.

Compared with the total particle size distribution, the peak values of the six main particle types show minor differences (< 80 nm) during the two different episode periods (Fig. 11b,c). However, the percentage of the six particle types distribute in wider size ranges during E2 than during E1 possibly due to the more intensive atmospheric aging. Similarly, during the two episodes (Fig. 3b,c), the relatively high fraction of the rich-K and BB particles are more affected by the primary emissions when their peak value concentrate at < 300 nm, and > 300 nm are more related to the aging process (Li et al., 2022b; Bi et al., 2011). Relatively greater fluctuation for the large-size fractions (> 1.1 μm) could be explained by the low particle concentration (a number less than 20). It should be pointed out that further application of this method would require a co-located particle-sizing instrument to scale the size-resolved particle detection efficiency. Both particle composition and size-dependent are the predominant impacting factors on the particle detection efficiency of the SPAMS (Wenzel et al., 2003; Yang et al., 2017; Healy et al., 2013).

To investigate the mixing state of the secondary species in the six main particle types, the number fractions of six secondary markers ($^{97}HSO_4^-$, $^{195}H(HSO_4)_2^-$, $^{62}NO_3^-$, $^{18}NH_4^+$, $^{58}C_2H_5NHCH_2^+$ and $^{89}HC_2O_4^-$) are calculated (Fig. 4). The presences of amine (*m/z* $^{58}C_2H_5NHCH_2^+$) and sulfuric acid (*m/z* $^{195}H(HSO_4)_2^-$) signals are possibly indicative of the water uptake (Chen et al., 2019) and acidic property of the particles (Rehbein et al., 2011), respectively. The mixing states are obtained by the ratio of the number concentration of the selected ions to each particle type.

The most abundant of $^{97}HSO_4^-$ and $^{18}NH_4^+$ fraction are seen in Ammonium (99% and 94%, *respectively*) and EC-aged (92% and 31%, *respectively*) particles, whereas much low fraction of $^{62}NO_3^-$ is found (2% and 7%, *respectively*). These suggest that ammonium sulfate is not a predominant form instead of ammonium nitrate (Zhang et al., 2013). The high contribution of $^{97}HSO_4^-$ in EC-containing particles also suggests a significant influence of anthropogenically emitted sulfate precursors (e.g., $SO_2$) on the aging of EC-containing particles at the high altitude (Peng et al., 2016; Zhang et al., 2017a). Meanwhile, relatively high number fractions of $^{195}H(HSO_4)_2^-$ and $^{58}C_2H_5NHCH_2^+$ are also observed in Ammonium (63% and 60%) and EC-aged (4% and 19%) particles. These abundant mixtures potentially represent the high hygroscopicity of Ammonium and EC-aged particles, and their ability to

neutralize the acidic particles of Ammonium particle (Sorooshian et al., 2007). Then, a moderate fraction of $^{97}HSO_4^-$ and $^{18}NH_4^+$ are seen on the rich-K (65%, 7%) and OC (56%, 4%) particles. In contrast, more $^{62}NO_3^-$ fraction contribute to the rich-K (38%) and OC (68%) particles, mainly affected by vehicle emissions and biomass burning (Text S1). Following BB (18%) and Dust (6%) particles are found in a relatively low fraction of $^{97}HSO_4^-$, while the moderate $^{62}NO_3^-$ accounts for 45% of the BB particle but only 3% of the Dust particle. Combined with the results of the minor $^{18}NH_4^+$ fraction (<1%) in BB and Dust particles suggests a relatively low degree of aging. In addition, oxalate ($^{89}HC_2O_4^-$), a representative component of secondary organic formation is mainly mixed with BB (13%) and rich-K (12%) particles. This is because the substantial precursors of oxalic acid, including acetate ($^{59}C_2H_3O_2^-$), methylglyoxal ($^{71}C_3H_3O_2^-$), glyoxylate ($^{73}C_2HO_3^-$), are emitted from biomass burning, and then oxalate heterogeneously formed in BB related particles (Zhang et al., 2019b; Zauscher et al., 2013). A relatively low fraction (<5%) of oxalate-containing particles in OC, Ammonium, EC-aged and Dust particles is potentially limited by the contributions of precursor oxalic acid.

Compared to the mixing state of individual particle in urban or suburban areas that are located close to emission sources (Chen et al., 2016; Dall′Osto and Harrison, 2012; Zhang et al., 2017a; Li et al., 2022b), the high fractions of sulfate and ammonium at the high altitude area demonstrate a high degree of aging of the individual particles, whereas the low fraction of nitrate with high volatility indicates its loss during transportation processing.

The number fractions of six markers in the four trajectories were used to further investigate the impacts of regional transport. As shown in Fig. 5(a,c), the dominant mixing ion types in each particles (except for Dust) are similar among the four clusters. For Cluster 1, the number fractions of $^{97}HSO_4^-$ and $^{89}HC_2O_4^-$ have larger values in five particle types (except for Dust type) than those in other trajectories. Similar to Cluster 1, Cluster 3 and 4 are impacted by regional transport from northeastern Myanmar, the fractions of the six markers also similar in OC, Ammonium, and EC-aged types. However, $^{97}HSO_4^-$ in Cluster 3 and 4 is reduced in rich-K, BB and Dust types, while $^{62}NO_3^-$ is increased in rich-K and decreased in Dust types, compared with Cluster 1. As discussed in Section 3.1, these results demonstrate that the aging degree of Cluster 3 and 4 might be lower than that of Cluster 1. For Cluster 2,

the fraction of $^{97}HSO_4^-$ is obviously decreased in rich-K, BB and EC-aged types but slightly increased in Dust type (Fig. 5f). Such pattern inverse the observations in rich-K, OC and Dust types for $^{62}NO_3^-$ ions. These variations in Cluster 2 are more likely due to the influences of biomass-burning activities from surrounding the sampling site, rather than regional transport. Furthermore, Cluster 2 is associated with regional transport from northeastern India along the afternoon to nighttime (from 15:00 LT on 11 May to 07:00 LT on 12 May), which is favorable to the nitrate formation $N_2O_5$ by heterogeneous hydrolysis (Wang et al., 2017; Ding et al., 2021). However, these cases are infrequent, as only 2% of trajectories are associated with Cluster 2.

During E1, more than 50% of $^{97}HSO_4^-$ fractions are mixed in the rich-K (81%), OC (62%), Ammonium (100%), EC-aged (98%) particles (Fig. S12), low in BB (37%) and Dust (4%) particles. Dissimilar with E1, the number fraction of $^{97}HSO_4^-$ in Dust increases to 34% during E2, potentially associated with the enhancement by secondary formation during regional transport. However, the mixing state of $^{195}H(HSO_4)_2^-$), $^{62}NO_3^-$, $NH_4^+$ and oxalate fractions are similar between the two episode events. The $^{58}C_2H_5NHCH_2^+$ fractions are significantly higher in E2 than E1 for Ammonium (67% versus 31%) and EC-aged particles (48% versus 17%), due to the relatively higher hygroscopic behavior (i.e., RHs) (Sorooshian et al., 2007).

### 3.3 Formation process of the high number concentration particle episodes

Photochemical oxidation and aqueous-phase reaction are the key formation pathways of secondary species (Link et al., 2017; Xue et al., 2014; Jiang et al., 2019). The oxidant $O_x$ ($O_3$ + $NO_2$) concentration and RH usually serve as indicators of the degree of photochemical oxidation (Wood et al., 2010) and aqueous-phase reaction (Ervens et al., 2011), *receptively,* though the current $O_x$ and RH conditions obtained using the in-situ measurement are not indicative of the past conditions experienced by the particle. Thus, the relative number fractions of $^{43}C_2H_3O^+$, $^{89}HC_2O_4^-$, $^{62}NO_3^-$, $^{97}HSO_4^-$ and $^{18}NH_4^+$-containing particles to the total detected particles were selected to provide a rough speculative of the secondary formation mechanism in TP ambient conditions (Liang et al., 2022). The correlations of the number fraction of each secondary species with the $O_x$ concentrations ($O_x$) during daytime (from 06:00 to 20:00 LT) and RH during nighttime (from 20:00 to 06:00 LT next day) are used to

reveal the formation pathways during the two episodes (Li et al., 2022).

As illustrated in Fig. 6, for E1, $^{43}C_2H_3O^+$, $^{89}HC_2O_4^-$, $^{97}HSO_4^-$, and $^{18}NH_4^+$ show significant negative linear correlations with $O_x$ ($p < 0.01$), and the correlation strengths range from moderate to strong (r = –0.51 to –0.81). However, the $^{62}NO_3^-$ fraction shows an upward trend with an insignificant correlation (r = 0.33, $p > 0.05$) with the increase in $O_x$ concentration. For E2, $^{43}C_2H_3O^+$ shows weak correlation with $O_x$ (r = 0.37, $p > 0.05$), but strong correlations with $^{89}HC_2O_4^-$, $^{97}HSO_4^-$, and $^{18}NH_4^+$ (r = 0.81~0.92, $p < 0.01$). It should be noted that $^{62}NO_3^-$ has a strong negative correlation (r =–0.85, $p < 0.01$) with $O_x$. In general, the opposite linear relationship between secondary aerosol and $O_x$ during E1 and E2 might be influenced by reasons of i) the relatively low secondary formations because of the small amount of precursors emitting from anthropogenic activities around the sampling site (Li et al., 2016); ii) higher dilution rate of the particles formed in the atmosphere with the rapid rise of PBL height during E1 than E2 (Fig. S13a); iii) the degrees of contributions of regional transport due to the low WS (0.5 ± 0.6 m $s^{-1}$) during E1 and the high WS (3.1 ± 1.0 m $s^{-1}$) during E2, respectively (Fig. S9). Therefore, for E1, the increases of $NO_3^-$ fraction could be influenced by the local nitrate formation, while the declines of other secondary components should be ascribed to the reduced contribution of regional transport. For E2, the decreased of $NO_3^-$ fraction could be caused by the relatively higher volatilization loss of nitrate than other components through the regional transport. Additionally, previous study proves that the formations of organic nitrate species (such as $^{27}CHN^+$, $^{30}NO^+$, $^{43}CHO_1N^+$ and $CHO_xN^+$) through the NO+$RO_2$ pathway dominate 80% of the total nitrate production in tropical forested regions during summertime (Alexander et al., 2009). Aruffo et al (2022) also found that low $NO_x$ (i.e. < 6 ppbv), compared to 2.3 ± 0.8 ppbv in this study, could even promote the particle-phase partitioning of the lower volatility of organonitrates. These results suggest that the secondary organic species have different formation capacities through photo-oxidation reactions, among which the rate of $HSO_4^-$ formation (slop=0.017) is the highest. Increased with $O_x$ concentration during E2, the concentration levels of secondary organic species of $C_2H_3O^+$ (18%-28%) imperceptibly rise, while the oxalate fraction significantly increase by 7%-20%.

Considering that the oxalate is abundant mixed in rich-K (14%), BB (15%), EC-aged

(5%), and Dust (6%) particles in Cluster 1 (Fig. 5), and the increased contributions of rich-K (39.3%), BB (14.2%) and EC-aged (17.2%) types during E2 (Table 1), the apparent formation of oxalate might be due to the enhancement of regional transport. Particularity, this presents the nearby biomass burning and combustion activities produce more precursor species of oxalate (Sullivan et al., 2007; Kundu et al., 2010; Zhang et al., 2017b).

Fig. 7 illustrates that the number fractions of $^{43}C_2H_3O^+$, $^{89}HC_2O_4^-$, $^{97}HSO_4^-$, and $^{18}NH_4^+$ have moderate to strong positive correlations with RH (r = 0.70~0.81, $p < 0.01$ or 0.05) in the nighttime during the two episodes, except that $^{43}C_2H_3O^+$ during E2 ($p = 0.48$) and $^{89}HC_2O_4^-$ during E1 ($p = 0.12$). Furthermore, $^{62}NO_3^-$ fraction has no obvious changes with insignificant correlation with RH during E1 ($p = 0.43$) and presents a moderate negative correlation with RH (r = 0.69, $p < 0.01$) during E2. As shown in Fig. 7e, the highest aqueous formation rate of $HSO_4^-$ is mainly due to the properties of low volatile and high hygroscopic of sulfate (Wang et al., 2016; Zhang et al., 2019c; Sun et al., 2013). Compared with that during E2 (slop=0.014), the decreased formation rate of $HSO_4^-$ during the E1 (slop=0.009) may be because the decreases of aerosol acidity in higher RH > 80% (Huang et al., 2019; Meng et al., 2014; Tian et al., 2021). And the increased contributions of regional transport due to the high WS (2.4 ± 0.8 m $s^{-1}$) during E2 are compared with the low WS (0.08 ± 0.08 m $s^{-1}$) during E1 (Fig. S9). The fair production rate of $NH_4^+$ during the E1 (slop= 0.005) and E2 (slop=0.006) demonstrate that an aqueous-phase reaction could effectively promote ammonium formation. Meanwhile, a slightly larger slop of $NH_4^+$ during E2 could be also affected by the increased contributions of regional transport. Compared with those during E1, the inverse generation rates of two secondary organic species (i.e., $C_2H_3O^+$ and $HC_2O_4^-$) during E2 are possibly caused by the different formation pathways with a variety of RH levels or distinct regional transports. For example, $C_2H_3O^+$ shows a strong correlation with RH (r = 0.70, $p < 0.05$) during E1 (slop=0.003) but has insignificant correlation during E2. This could be explained by high RHs that could effectively promote secondary organic formation during E1. In addition, the $HC_2O_4^-$ fraction increases slightly (9.7-13.1%) during E1 is potentially ascribed to more abundant Dust-type particles (20.3%) which compose of high calcium (Ca) (Fig. S14) that favor the formation of metal oxalate complexes (i.e., Ca oxalate). At high RHs (93.4 ± 7.6%), if oxalate ions are dissolved in the aqueous phase with the presence of Ca ions, the Ca

oxalate complexes can precipitate because of their low hygroscopic and insoluble natures (Furukawa and Takahashi, 2011). This could offset the oxalate formation in the aqueous-phase reaction. However, significant linear increases (slop=0.003) with RH ($r = 0.81$, $p < 0.01$) during E2 demonstrate that the aqueous-phase reaction effectively promotes the oxalate formation (Cheng et al., 2017; Meng et al., 2020). No obvious change and insignificant correlation between $^{62}NO_3^-$ and RH are found during E1, potentially attributed to the decreases of $NO_2$ concentration (3.7 ± 0.4 ppbv) in the local atmosphere. Meanwhile, high RHs could promote organonitrates formation (Fang et al., 2021; Fry et al., 2014). The linearity between $^{62}NO_3^-$ and RH ($r = 0.69$, $p < 0.01$) significantly decreases during E2, mostly due to the losses of the volatile compound through the regional transport (Fig. S15).

## 4 Conclusions

This study presents the chemical composition, size distribution, mixing state and secondary formation of individual particles in the southeastern margin of TP, China during the pre-monsoon season using a high-resolution SPAMS. The finding shows that the rich-K (30.9%) and BB types (18.7%) are the two dominant aerosol particles in the remote area; followed by the OC (12.8%), Ammonium (11.9%), EC-aged (10.9%), and Dust (10.7%) types; the NaK-SN, Metal and Others particle types contributed 0.3–2.8% to the total ambient particles. By interpreting the mass spectra and diurnal trends, the major particle types are mainly from traffic emission, biomass burning, secondary formation and fly ash, while the dynamics of the PBL height could also affect their contributions. The observed change in the number fraction of the particle types was mainly influenced by air mass (97.61% of the total trajectories) from northeastern Myanmar, and significantly contributed to rich-K and BB types. The particle types show distinct size distributions. The two critical particle types of rich-K and BB appear in a unimodal pattern, the fractions of OC and EC-aged gradually decrease with the increase of the particle sizes, but Ammonium and Dust types show the opposite. Sulfate is the major secondary species and is highly mixed with rich-K, Ammonium and EC-aged types. Nitrate has a relatively low mixing ratio due to its higher volatility than sulfate during regional transportation, except for BB and OC types. During the entire study campaign, two episodes with the high number concentration of particles occur but with significant differences in each particle fraction due to the different meteorological conditions

(RH, WS, etc.). Meanwhile, the different meteorological conditions also lead to an inverse linear correlation between the indicators of secondary formation, including $C_2H_3O^+$, $HC_2O_4^-$, $NH_4^+$, $NO_3^-$ and $HSO_4^-$. and $O_x$ ($O_3$+$NO_2$) during episode 1 and 2 periods; however, they present a positive linear correlation with relative humidity (RH), except for $NO_3^-$ shown the negative linear correlation with RH due to the low precursors concentration and potential organonitrates formation. These results demonstrated that the capacity of atmospheric aging of photo-oxidation and aqueous reaction have complex influencing factors. Although the detailed formation pathways and their percentage contributions to secondary species are not quantitatively estimated in this study, our results have important implications for the various possibilities affecting the characteristic of chemical components, size distribution, mixing states, and formation mechanism of aerosols in the southeast TP. More depth investigations concerning the evolution mechanisms of secondary aerosols are encouraged since TP is a significant regulator to global climate change.

*Data availability*. The data presented in this study are available at the Zenodo data archive https://doi.org/10.5281/zenodo.7336857.

*Competing interests*. The authors declare that they have no conflict of interest.

*Author contributions*. QW and JC designed the campaign. WR conducted field measurements. LL, QW, JT, and YZ made data analysis and interpretation. LL and QW wrote the paper. All the authors reviewed and commented on the paper.

*Acknowledgments*. The authors are grateful to the staff from Lijiang Astronomical Station for their assistance with field sampling. The authors are also grateful to Weikang Ran, Yonggang Zhang, and other staff for the field observation.

*Financial support*. This work was supported by the Second Tibetan Plateau Scientific Expedition and Research Program (STEP) (2019QZKK0602), the National Natural Science Foundation of China (41877391), and the Youth Innovation Promotion Association of the Chinese Academy of Sciences (2019402).

## Reference

Alexander, B., Hastings, M. G., Allman, D. J., Dachs, J., Thornton, J. A., and Kunasek, S. A.: Quantifying atmospheric nitrate formation pathways based on a global model of the oxygen isotopic composition ($\Delta^{17}O$) of atmospheric nitrate, Atmos. Chem. Phys., 9, 5043–5056, https://doi.org/10.5194/acp-9-5043-2009, 2009.

Aruffo, E., Wang, J., Ye, J., Ohno, P., Qin, Y., Stewart, M., McKinney, K., Di Carlo, P., and Martin, S. T.: Partitioning of Organonitrates in the Production of Secondary Organic Aerosols from α-Pinene Photo-Oxidation, Environ. Sci. Technol., 56, 5421–5429, https://doi.org/10.1021/acs.est.1c08380, 2022.

Bi, X. H., Zhang, G. H., Li, L., Wang, X. M., Li, M., Sheng, G. Y., Fu, J. M., and Zhou, Z.: Mixing state of biomass burning particles by single particle aerosol mass spectrometer in the urban area of PRD, China, Atmos. Environ., 45, 3447–3453, https://doi.org/10.1016/j.atmosenv.2011.03.034, 2011.

Bi, X. H., Lin, Q. H., Peng, L., Zhang, G. H., Wang, X. M., Brechtel, F. J., Chen, D. H., Li, M., Peng, P. A., Sheng, G. Y., and Zhou, Z.: In situ detection of the chemistry of individual fog droplet residues in the Pearl River Delta region, China, J. Geophys. Res. Atmos., 121, 9105–9116, https://doi.org/10.1002/2016jd024886, 2016.

Budisulistiorini, S. H., Riva, M., Williams, M., Chen, J., Itoh, M., Surratt, J. D., and Kuwata, M.:

Light-absorbing brown carbon aerosol constituents from combustion of Indonesian peat and biomass, Environ. Sci. Technol., 51, 4415-4423, https://doi.org/10.1021/acs.est.7b00397, 2017.

Canagaratna, M. R., Jayne, J. T., Jimenez, J. L., Allan, J. D., Alfarra, M. R., Zhang, Q., Onasch, T. B., Drewnick, F., Coe, H., Middlebrook, A., Delia, A., Williams, L. R., Trimborn, A. M., Northway, M. J., DeCarlo, P. F., Kolb, C. E., Davidovits, P., and Worsnop, D. R.: Chemical and microphysical characterization of ambient aerosols with the aerodyne aerosol mass spectrometer, Mass Spectrom. Rev., 26, 185–222, https://dx.doi.org/10.1002/mas.20115, 2007.

Chan, C. Y., Wong, K. H., Li, Y. S., Chan, Y., and Zhang, X.D.: The effects of Southeast Asia fire activities on tropospheric ozone, trace gases and aerosols at a remote site over the Tibetan Plateau of Southwest China, Tellus B, 58B, 310–318, https://doi.org/10.1111/j.1600-0889.2006.00187.x, 2017.

Chen, Y., Cao, J. J., Huang, R. J., Yang, F. M., Wang, Q. Y., and Wang, Y. C.: Characterization, mixing state, and evolution of urban single particles in Xi'an (China) during wintertime haze days, Sci. Total Environ., 573, 937–945, https://doi.org/10.1016/j.scitotenv.2016.08.151, 2016.

Chen, Y., Wenger, J. C., Yang, F. M., Cao, J. J., Huang, R. J., Shi, G. M., Zhang, S. M., Tian, M., and Wang, H. B.: Source characterization of urban particles from meat smoking activities in Chongqing, China using single particle aerosol mass spectrometry, Environ. Pollut., 228, 92–101, https://doi.org/10.1016/j.envpol.2017.05.022, 2017.

Chen, Y., Tian, M., Huang, R. J., Shi, G. M., Wang, H. B., Peng, C., Cao, J. J., Wang, Q. Y., Zhang, S. M., Guo, D. M., Zhang, L. M., and Yang, F. M.: Characterization of urban amine-containing particles in southwestern China: seasonal variation, source, and processing, Atmos. Chem. Phys., 19, 3245–3255, https://doi.org/10.5194/acp-19-3245-2019, 2019.

Chen, J. Q., and Bordoni, S.: Orographic effects of the Tibetan Plateau on the East Asian Summer Monsoon: An energetic perspective, J. Climate., 27, 3052–3072, https://doi.org/10.1175/JCLI-D-13-00479.1, 2014.

Cheng, C. L., Li, M., Chan, C. K., Tong, H. J., Chen, C. H., Chen, D. H., Wu, D., Li, L., Wu, C., Cheng, P., Gao, W., Huang, Z. X., Li, X., Zhang, Z. J., Fu, Z., Bi, Y. R., Zhou, Z.: Mixing state of acid containing particles in the rural area of Pearl River Delta, China: implicatio the formation mechanism of oxalic acid, Atmos. Chem. Phys., 17, 9519–9533, https://doi.org/10.5194/acp-17-9519-2017, 2017.

Crippa, M., DeCarlo, P. F., Slowik, J. G., Mohr, C., Heringa, M. F., Chirico, R., Poulain, L., Freutel, F., Sciare, J., Cozic, J., Di Marco, C. F., Elsasser, M., Nicolas, J. B., Marchand, N., Abidi, E., Wiedensohler, A., Drewnick, F., Schneider, J., Borrmann, S., Nemitz, E., Zimmermann, R., Jaffrezo, J. L., Prévôt, A. S. H., and Baltensperger, U.: Wintertime aerosol chemical composition and source apportionment of the organic fraction in the metropolitan area of Paris, Atmos. Chem. Phys., 13, 961–981, https://doi.org/10.5194/acp-13-961-2013, 2013.

Dall'Osto, M., Beddows, D.C.S., Gietl, J. K., Olatunbosun, O. A., Yang, X. G., and Harrison, R. M.: Characteristics of tyre dust in polluted air: studies by single particle mass spectrometry (ATOFMS), Atmos. Environ., 94, 224–230, https://doi.org/10.1016/j.atmosenv.2014.05.026, 2014.

Dall'Osto, M., and Harrison, R. M.: Urban organic aerosols measured by single particle mass spectrometry in the megacity of London, Atmos. Chem. Phys., 12, 4127–4142, http://dx.doi.org/10.5194/acp-12-4127–2012, 2012.

Ding, J., Dai, Q. L., Zhang, Y. F., Xu, J., Huangfu, Y. Q., Feng, Y. C.: Air humidity affects secondary aerosol formation in different pathways, Sci. Total Environ., 759, 143540–143549, https://doi.org/10.1016/j.scitotenv.2020.143540¸ 2021.

Draxler, R. and Hess, G.: An overview of the HYSPLIT_4 modelling system for trajectories, Aust.

Meteorol. Mag., 47, 295–308, 1998.
Du, W., Sun, Y. L., Xu, Y. S., Jiang, Q., Wang, Q. Q., Wang, W., Wang, F., Bai, Z. P., Zhao, X. D., and Yang, Y. C.: Chemical characterization of submicron aerosol and particle growth events at a national background site (3295 m a.s.l.) on the Tibetan Plateau, Atmos. Chem. Phys., 15, 10811–10824, https://doi.org/10.5194/acp-15-10811-2015, 2015.
Engling, G., Zhang, Y. N., Chan, C. Y., Sang, X. F., Lin, M., Ho, K. F., Li, Y. S., Lin, C. Y., and Lee, J. J.: Characterization and sources of aerosol particles over the southeastern Tibetan Plateau during the Southeast Asia biomass-burning season, Tellus B, 63, 117–128, https://doi.org/10.1111/j.1600-0889.2010.00512.x, 2011.
Ervens, B., Turpin, B. J., and Weber, R. J.: Secondary organic aerosol formation in cloud droplets and aqueous particles (aqSOA): a review of laboratory, field and model studies, Atmos. Chem. Phys., 11, 11069–11102, https://doi.org/10.5194/acp-11-11069-2011, 2011.
Fang, X. Z., Liu, Y. Y., Li, K. J., Wang, T., Deng, Y., Feng, Y. Q., Yang, Y., Cheng, H. Y., Chen, J. M., and Zhang, L. W.: Atmospheric Nitrate Formation through Oxidation by Carbonate Radical, ACS Earth Space Chem., 5, 1801–1811, https://doi.org/10.1021/acsearthspacechem.1c00169, 2021.
Fry, J. L., Draper, D. C., Barsanti, K. C., Smith, J. N., Ortega, J., Winkler, P. M., Lawler, M. J., Brown, S. S., Edwards, P. M., Cohen, R. C., and Lee, L.: Secondary Organic Aerosol Formation and Organic Nitrate Yield from $NO_3$ Oxidation of Biogenic Hydrocarbons, Environ. Sci. Technol., 48, 11944–11953, https://doi.org/10.1021/es502204x, 2014.
Furukawa, T., and Takahashi, Y.: Oxalate metal complexes in aerosol particles: implications for the hygroscopicity of oxalate-containing particles, Atmos. Chem. Phys., 11, 4289–4301, https://doi.org10.5194/acp-11-4289-2011, 2011.
Gettelman, A., Morrison, H., Terai, C. R., and Wood, R.: Microphysical process rates and global aerosolecloud interactions, Atmos. Chem. Phys., 13, 9855–9867, https://doi.org/10.5194/acp-14-9099-2014, 2013.
Han, H., Wu, Y., Liu, J., Zhao, T. L., Zhuang, B. L., Wang, H. L., Li, Y. C., Chen, H. M., Zhu, Y., Liu, H. N., Wang, Q. G., Li, S., Wang, T. J., Xie, M., and Li, M. M.: Impacts of atmospheric transport and biomass burning on the inter-annual variation in black carbon aerosols over the Tibetan Plateau, Atmos. Chem. Phys., 20, 13591–13610, https://doi.org/10.5194/acp-20-13591-2020, 2020.
Healy, R. M., Sciare, J., Poulain, L., Crippa, M., Wiedensohler, A., Prévôt, A.S.H., Baltensperger, U., Sarda-Estève, R., McGuire, M. L., Jeong, C. H., McGillicuddy, E., O'Connor, I. P., Sodeau, J. R., Evans, G. J., and Wenger, J. C.: Quantitative determination of carbonaceous particle mixing state in Paris using single-particle mass spectrometer and aerosol mass spectrometer measurements, Atmos. Chem. Phys., 13, 9479–9496, http://dx.doi.org/10.5194/acp-13-9479-2013, 2013.
Hua, S., Liu, Y. Z., Luo, R., Shao, T. B., Zhu, Q. Z.: Inconsistent aerosol indirect effects on water clouds and ice clouds over the Tibetan Plateau, Int. J. Climatol., 40, 3832–3848, https://doi.org/10.1002/joc.6430, 2019.
Huang, X. J., Zhang, J. K., Luo, B., Luo, J. Q., Zhang, W., and Rao, Z. H.: Characterization of oxalic acid-containing particles in summer and winter seasons in Chengdu China, Atmos. Environ., 198, 133–141, https://doi.org/10.1016/j.atmosenv.2018.10.050, 2019.
Immerzeel, W. W., van Beek, L. P. H., and Bierkens, M. F. P.: Climate change will affect the Asian water towers, Science, 328, 1382–1385, https://doi.org/10.1126/science.1183188, 2010.
Jacobson, M. Z.: Analysis of aerosol interactions with numerical techniques for solving coagulation, nucleation, condensation, dissolution, and reversible chemistry among multiple size distributions, J.

Geophys. Res., 107(D19), 4366, https://doi.org/10.1029/2001JD002044, 2002.
Jiang, H. H., Frie, A. L., Lavi, A., Chen, J. Y., Zhang, H., Bahreini, R., and Lin, Y. H.: Brown carbon formation from nighttime chemistry of unsaturated heterocyclic volatile organic compounds, Environ. Sci. Technol. Lett., 6, 184190, https://doi.org/10.1021/acs.estlett.9b00017, 2019.
Kumar, M., Raju, M. P., Singh, R. K., Singh, A. K., Singh, R. S., and Banerjee, T.: Wintertime characteristics of aerosols over middle Indo-Gangetic Plain: vertical profile, transport and radiative forcing, Atmos. Res., 183, 268–282, https://doi.org/10.1016/j.atmosres.2016.09.012, 2017.
Kundu, S., Kawamura, K., Andreae, T. W., Hoffer, A., and Andreae, M. O.: Molecular distributions of dicarboxylic acids, ketocarboxylic acids and alpha-dicarbonyls in biomass burning aerosols: implications for photochemical production and degradation in smoke layers, Atmos. Chem. Phys., 10 (5), 2209−2225, https://doi.org/10.5194/acp-10-2209-2010, 2010.
Lian, X. F., Zhang, G. H., Yang, Y. X., Lin, Q. H., Fu, Y. Z., Jiang, F., Peng, L., Hu, X. D., Chen, D. H., Wang, X. M., Peng, P. A., Sheng, G. Y., and Bi, X. H.: Evidence for the Formation of Imidazole from Carbonyls and Reduced Nitrogen Species at the Individual Particle Level in the Ambient Atmosphere, Environ. Sci. Technol. Lett., 8, 9–15, https://dx.doi.org/10.1021/acs.estlett.0c00722, 2021.
Liang, Z. C., Zhou, L. Y., Cuevas, R. A., Li, X. Y., Cheng,C. L., Li, M., Tang, R. Z., Zhang, R. F., Lee Patrick K. H., Lai, Alvin C. K., and Chan, C.K.: Sulfate Formation in Incense Burning Particles: A Single-Particle Mass Spectrometric Study, Environ. Sci. Technol. Lett., 9, 718–725, https://doi.org/10.1021/acs.estlett.2c00492, 2022.
Li, C. L., Bosch, C., Kang, S. C., Andersson, A., Chen, P. F., Zhang, Q. G., Cong, Z. Y., Chen, B., Qin, D. H., and Gustafsson., Ö.: Sources of black carbon to the Himalayan–Tibetan Plateau glaciers, Nat. Commun., 7, 12574, https://doi.org/10.1038/ncomms12574, 2016b.
Li, C. L., Bosch, C., Kang, S. C., Andersson, A., Chen, P. F., Zhang, Q. G., Cong, Z. Y., Tripathee, L., and Örjanb, G.: $^{14}C$ characteristics of organic carbon in the atmosphere and at glacier region of the Tibetan Plateau, Sci. Total Environ., 832, 155020, https://doi.org/10.1016/j.scitotenv.2022.155020, 2022a.
Li, L., Huang, Z. X., Dong, J. G., Li, M., Gao, W., Nian, H. Q., Fu, Z., Zhang, G. H., Bi, X. H., Cheng, P., and Zhou, Z.: Real time bipolar time-of-flight mass spectrometer for analyzing single aerosol particles, Int. J. Mass Spectrom., 303, 118–124, https://doi.org/10.1016/j.ijms.2011.01.017, 2011.
Li L., Wang, Q. Y., Zhang, Y., Liu, S. X., Zhang, T., Wang, S., Tian, J., Chen, Y., Hang Ho, S. S., Han, Y., and Cao, J.J.: Impact of reduced anthropogenic emissions on chemical characteristics of urban aerosol by individual particle analysis, Chemosphere, 303, 135013, https://doi.org/10.1016/j.chemosphere.2022.135013, 2022b.
Li, J. J., Wang, G. H., Wang, X. M., Cao, J. J., Sun, T., Cheng, C. L., Meng, J. J., Hu, T. F., and Liu, S. X.: Abundance, composition and source of atmospheric $PM_{2.5}$ at a remote site in the Tibetan Plateau, China, Tellus B, 65, http://dx.doi.org/10.3402/tellusb.v65i0.20281, 2013.
Li, Y. J., Sun, Y. L., Zhang, Q., Li, X., Li, M., Zhou, Z., and Chan, C. K.: Real-time chemical characterization of atmospheric particulate matter in China: A review, Atmos. Environ., 158, 270–304, http://dx.doi.org/10.1016/j.atmosenv.2017.02.027, 2017.
Lin, Q. H., Bi, X. H., Zhang, G. H., Yang, Y. X., Peng, L., Lian, X. F., Fu, Y. Z., Li, M., Chen, D. H., Miller, M., Ou, J., Tang, M. J., Wang, X. M., Peng, P. A., Sheng, G. Y., and Zhou, Z.: In-cloud formation of secondary species in iron-containing particles, Atmos. Chem. Phys., 19, 1195–1206, https://doi.org/10.5194/acp-19-1195-2019, 2019.
Link, M. F., Kim, J., Park, G., Lee, T., Park, T., Babar, Z. B., Sung, K., Kim, P., Kang, S., Kim, J. S., Choi, Y., Son, J., Lim, H. J., and Farmer, D.K.: Elevated production of $NH_4NO_3$ from the photochemical

665 processing of vehicle exhaust: Implications for air quality in the Seoul Metropolitan Region, Atmos.
666 Environ., 156, 95–101, https://doi.org/10.1016/j.atmosenv.2017.02.031, 2017.
667 Liu, Y. Z., Zhu, Q. Z., Huang, J. P., Hua, S., and Jia, R.: Impact of dust-polluted convective clouds over the
668 Tibetan Plateau on downstream precipitation, Atmos. Environ., 209, 67–77,
669 https://doi.org/10.1016/j.atmosenv.2019.04.001, 2019.
670 Liu, Q., Liu, D. T., Gao, Q., Tian, P., Wang, F., Zhao, D. L., Bi, K., Wu, Y. Z., Ding, S., Hu, K., Zhang, J.
671 L., Ding, D. P., and Zhao, C. S.: Vertical characteristics of aerosol hygroscopicity and impacts on
672 optical properties over the North China Plain during winter, Atmos. Chem. Phys., 20, 3931–3944,
673 https://doi.org/10.5194/acp-20-3931-2020, 2020a.
674 Liu, D. T., Hu, K., Zhao, D. L., Ding, S., Wu, Y. F., Zhou, C., Yu, C. J., Tian, P., Liu, Q., Bi, K., Wu, Y. Z.,
675 Hu, B., Ji, D. S., Kong, S. F., Ouyang, B., He, H., Huang, M. Y., and Ding, D.P.: Efficient Vertical
676 Transport of Black Carbon in the Planetary Boundary Layer, Geo. Res. Lett., 47, 1–10, https://doi.org/
677 10.1029/2020GL088858, 2020b
678 Liu, H. K., Wang, Q. Y., Xing, L., Zhang, Y., Zhang, T., Ran, W. K., and Cao, J. J.: Measurement report:
679 quantifying source contribution of fossil fuels and biomass-burning black carbon aerosol in the
680 southeastern margin of the Tibetan Plateau, Atmos. Chem. Phys., 21, 973–987,
681 https://doi.org/10.5194/acp-21-973-2021, 2021.
682 Liu, X. D., Dong, B. W., Yin, Z. Y., Smith, R. S., Guo, Q. C.: Continental drift and plateau uplift control
683 origination and evolution of Asian and Australian monsoons, Sci. Rep., 7, 40344, https://doi.org/
684 10.1038/srep40344, 2017.
685 Luo, M., Liu, Y. Z., Zhu, Q. Z., Tang, Y. H., and Alam, K.: Role and mechanisms of black carbon affecting
686 water vapor transport to Tibet, Remote Sens., 12, 231, https://doi.org/10.3390/rs12020231, 2020.
687 Ma, L., Li, M., Huang, Z. X., Li, L., Gao, W., Nian, H. Q., Zou, L. L., Fu, Z., Gao, J., Chai, F. H., and
688 Zhou, Z.: Real time analysis of lead-containing atmospheric particles in Beijing during springtime by
689 single particle aerosol mass spectrometry, Chemosphere, 154, 454–462,
690 https://doi.org/10.1016/j.chemosphere.2016.04.001, 2016.
691 Ma, X., Yu, F., and Luo, G.: Aerosol direct radiative forcing based on GEOS-Chem-APM and uncertainties,
692 Atmos. Chem. Phys., 12, 5563–5581, https://doi.org/10.5194/acp-12-5563-2012, 2012.
693 Matsui, H.: Black carbon simulations using a size- and mixingstate-resolved three-dimensional model: 2.
694 Aging timescale and its impact over East Asia, J. Geophys. Res. Atmos., 121, 1808–1821,
695 https://doi.org/10.1002/2015jd023999, 2016.
696 Meng, J. J, Wang, G. H, Li, J. J, Cheng, C. L, Ren, Y. Q, Huang, Y., Cheng, Y. T, Cao, J. J, and Zhang, T.:
697 Seasonal characteristics of oxalic acid and related SOA in the free troposphere of Mt. Hua, central
698 China: implications for sources and formation mechanisms, Sci. Total Environ., 493, 1088–1097,
699 https://doi.org/10.1016/j.scitotenv.2014.04.086, 2014.
700 Meng, J. J., Liu, X. D., Hou, Z. F., Yi, Y. N., Yan, L., Li, Z., Cao, J.J., Li, J. J., Wang, G. H.: Molecular
701 characteristics and stable carbon isotope compositions of dicarboxylic acids and related compounds in
702 the urban atmosphere of the North China Plain: implications for aqueous phase formation of SOA
703 during the haze periods, Sci. Total Environ., 705, 135256,
704 https://doi.org/10.1016/j.scitotenv.2019.135256, 2020.
705 Ng, N. L., Canagaratna, M. R., Jimenez, J. L., Chhabra, P. S., Seinfeld, J. H., and Worsnop, D. R.: Changes
706 in organic aerosol composition with aging inferred from aerosol mass spectra, Atmos. Chem. Phys.,
707 11(13), 6465–6474, https://doi.org/10.5194/acp-11-6465-2011, 2011.
708 Peng, J. F., Hu, M., Guo, S., Du, Z. F., Zheng, J., Shang, D. J., Zamora, M. L., Zeng, L. M., Shao, M., Wu,

709 Y. S., Zheng, J., Wang, Y., Glen, C. R., Collins, D. R., Molina, M. J., and Zhang, R. Y.: Markedly
710 enhanced absorption and direct radiative forcing of black carbon under polluted urban environments,
711 P. Natl. Acad. Sci. USA, 113, 4266–4271, https://doi.org/10.1073/pnas.1602310113, 2016.
712 Pratt, K. A., Hatch, L. E., and Prather, K. A.: Seasonal volatility dependence of ambient particle phase
713 amines, Environ. Sci. Technol., 43, 5276–5281, https://doi.org/10.1021/es803189n, 2009.
714 Pratt, K. A., Murphy, S. M., Subramanian, R., DeMott, P. J., Kok, G. L., Campos, T., Rogers, D. C., Prenni,
715 A. J., Heymsfield, A. J., Seinfeld, J. H., and Prather, K. A.: Flight-based chemical characterization of
716 biomass burning aerosols within two prescribed burn smoke plumes, Atmos. Chem. Phys., 11,
717 12549–12565, https://doi.org/10.5194/acp-11-12549-2011, 2011.
718 Qian, Y., Flanner, M. G., Leung, L. R., and Wang, W.: Sensitivity studies on the impacts of Tibetan Plateau
719 snowpack pollution on the Asian hydrological cycle and monsoon climate, Atmos. Chem. Phys., 11,
720 1929-1948, https://doi.org/10.5194/acp-11-1929-2011, 2011.
721 Rehbein, P. J., Jeong, C. H., McGuire, M. L., Yao, X., Corbin, J. C., and Evans, G. J.: Cloud and fog
722 processing enhanced gas-toparticle partitioning of trimethylamine, Environ. Sci. Technol., 45,
723 4346–4352, https://doi.org/10.1021/es1042113, 2011.
724 Roth, A., Schneider, J., Klimach, T., Mertes, S., van Pinxteren, D., Herrmann, H., and Borrmann, S.:
725 Aerosol properties, source identification, and cloud processing in orographic clouds measured by
726 single particle mass spectrometry on a central European mountain site during HCCT-2010, Atmos.
727 Chem. Phys., 16, 505–524, https://doi.org/10.5194/acp-16-505-2016, 2016.
728 Shen, L. J., Wang, H. L., Yin, Y., Chen, J. H., and Chen, K.: Observation of atmospheric new particle
729 growth events at the summit of mountain Tai (1534 m) in Central East China, Atmos. Environ., 201,
730 148–157, https://doi.org/10.1016/j.atmosenv.2018.12.051, 2019.
731 Shen, L. J., Wang, H. L., Lü, S., Zhang, X. H., Yuan, J., Tao, S. K., Zhang, G. J., Wang, F., and Li, L.:
732 Influence of pollution control on air pollutants and the mixing state of aerosol particles during the 2nd
733 World Internet Conference in Jiaxing, China, J. Clean. Prod., 149, 436–447,
734 https://doi.org/10.1016/j.jclepro.2017.02.114, 2017.
735 Shen, R. Q., Ding, X., He, Q. F., Cong, Z. Y., Yu, Q. Q., and Wang, X. M.: Seasonal variation of secondary
736 organic aerosol tracers in Central Tibetan Plateau, Atmos. Chem. Phys., 15, 8781-8793,
737 https://doi.org/10.5194/acp-15-8781-2015, 2015.
738 Sirois, A. and Bottenheim, J. W.: Use of backward trajectories to interpret the 5-year record of PAN and $O_3$
739 ambient air concentrations at Kejimkujik National Park, Nova Scotia, J. Geophys. Res., 100,
740 2867–2881, https://doi.org/10.1029/94JD02951, 1995.
741 Song, X. H., and Hopke, P. K.: Classifcation of single particles analyzed by ATOFMS using an artifcial
742 neural network, ART-2A, Anal. Chem., 71, 860–865, https://doi.org/10.1021/ac9809682, 1999.
743 Sorooshian, A., Lu, M. L., Brechtel, F. J., Jonsson, H., Feingold, G., Flagan, R. C., and Seinfeld, J. H.: On
744 the source of organic acid aerosol layers above clouds, Environ. Sci. Technol., 41, 4647–4654,
745 https://doi.org/10.1021/es0630442, 2007.
746 Sullivan, R. C., Guazzotti, S. A., Sodeman, D. A., and Prather, K. A.: Direct observations of the
747 atmospheric processing of Asian mineral dust, Atmos. Chem. Phys., 7, 1213–1236,
748 https://doi.org/10.5194/acp-7-1213-2007, 2007.
749 Sun, Y. L, Wang, Z. F., Fu, P. Q., Jiang, Q. J., Yang, T., Li, J., and Ge, X. L.: The impact of relative
750 humidity on aerosol composition and evolution processes during wintertime in Beijing, China, Atmos.
751 Environ., 77, 927–934, https://doi.org/10.1016/j.atmosenv.2013.06.019, 2013.
752 Tian, J., Wang, Q. Y., Zhang, Y., Yan, M. Y., Liu, H. K., Zhang, N. N., Ran, W. K., and Cao, J. J.: Impacts

753 of primary emissions and secondary aerosol formation on air pollution in an urban area of China
754 during the COVID-19 lockdown, Environ. Int., 150, 106426–14,
755 https://doi.org/10.1016/j.envint.2021.106426, 2021.
756 Wang, A. Q., Xie, X. N., Liu, X. D., and Yin, Z. Y.: Direct Radiative Effect (DRE) of Dust Aerosols on
757 West African and East Asian Monsoon: The Role of Ocean-Atmosphere Interactions, J. Geophys. Res.
758 Atmos., 127, 1–20, https://doi.org/10.1029/2021JD035917, 2022.
759 Wang, G. H., Zhang, R. Y., Gomez, M. E., Yang, L. X., Zamora, M. L., Hu, M., Lin, Y., Peng, J. F., Guo, S.,
760 Meng, J. J., Li, J. J., Cheng, C. L., Hu, T. F., Ren, Y. Q., Wang, Y. S., Gao, J., Cao, J. J., An, Z. S.,
761 Zhou, W. J., Li, G. H., Wang, J. Y., Tian, P. F., Marrero-Ortiz, W., Secrest, J., Du, Z. F., Zheng, J.,
762 Shang, D. J., Zeng, L. M., Shao, M., Wang, W. G., Huang, Y., Wang, Y., Zhu, Y. J., Li, Y. X., Hu, J. X.,
763 Pan, B. W., Cai, L., Cheng, Y. T., Ji, Y. M., Zhang, Y., Rosenfeld, D., Liss, P. S., Duce, R. A., Kolb, C.
764 E., and Molina., M. J.: Persistent sulfate formation from London Fog to Chinese haze, P. Natl. Acad.
765 Sci. USA, 113(48), 13630–13635, https://doi.org/10.1073/pnas.1616540113, 2016.
766 Wang, H. C., Lu, K. D., Chen, X. R., Zhu, Q. D., Chen, Q., Guo, S., Jiang, M. Q., Li, X., Shang, D. J., Tan,
767 Z. F., Wu, Y. S., Wu, Z. J., Zou, Q., Zheng, Y., Zeng, L. M., Zhu, T., Hu, M., Zhang, Y. H.: High
768 N2O5 concentrations observed in urban Beijing: implications of a large nitrate formation pathway,
769 Environ. Sci. Technol. Lett., 4, 416–420, https://doi.org/10.1021/acs.estlett.7b00341, 2017.
770 Wang, H. L., An, J. L., Shen, L. J., Zhu, B., Xia, L., Duan, Q., and Zou, J. N.: Mixing state of ambient
771 aerosols in Nanjing city by single particle mass spectrometry, Atmos. Environ., 132, 123–132,
772 https://dx.doi.org/10.1016/j.atmosenv.2016.02.032, 2016.
773 Wang, Q. Y., Han, Y. M., Ye, J. H., Liu, S. X., Pongpiachan, S., Zhang, N. N., Han, Y. M., Tian, J., Wu, C.,
774 Long, X., Zhang, Q., Zhang, W. Y., Zhao, Z. Z., and Cao, J. J.: High contribution of secondary brown
775 carbon to aerosol light absorption in the southeastern margin of Tibetan Plateau, Geophys. Res. Lett.,
776 46, 4962–4970, https://doi.org/10.1029/2019GL082731, 2019a.
777 Wang, H. L., Shen, L. J., Yin, Y., Chen, K., Chen, J. H., and Wang, Y. S.: Characteristics and mixing state
778 of aerosol at the summit of Mount Tai (1534 m) in Central East China: First measurements with
779 SPAMS, Atmos. Environ., 213, 273–284, https://doi.org/10.1016/j.atmosenv.2019.06.021, 2019b.
780 Wang, Q. Y., Cao, J. J., Han, Y. M., Tian, J., Zhu, C. S., Zhang, Y., Zhang, N. N., Shen, Z. X., Ni, H. Y.,
781 Zhao, S. Y., and Wu, J. R.: Sources and physicochemical characteristics of black carbon aerosol from
782 the southeastern Tibetan Plateau: internal mixing enhances light absorption, Atmos. Chem. Phys., 18,
783 4639–4656, https://doi.org/10.5194/acp-18-4639-2018, 2018.
784 Wenzel, R. J., Liu, D.-Y., Edgerton, E. S., and Prather, K. A.: Aerosol time-of-flight mass spectrometry
785 during the Atlanta Supersite Experiment: 2. Scaling procedures, J. Geophys. Res., 108, 8427,
786 http://dx.doi.org/10.1029/2001jd001563, 2003.
787 Wood, E. C., Canagaratna, M. R., Herndon, S. C., Onasch, T. B., Kolb, C. E., Worsnop, D. R., Kroll, J. H.,
788 Knighton, W. B., Seila, R., Zavala, M., Molina, L. T., DeCarlo, P. F., Jimenez, J. L., Weinheimer, A. J.,
789 Knapp, D. J., Jobson, B. T., Stutz, J., Kuster, W. C., and Williams, E. J.: Investigation of the
790 correlation between odd oxygen and secondary organic aerosol in Mexico City and Houston, Atmos.
791 Chem. Phys., 10, 8947–8968, https://doi.org/10.5194/acp-10-8947-2010, 2010.
792 Xu, L. L., Wu, X., Hong, Z. Y., Zhang, Y. R., Deng, J. J., Hong, Y. W., and Chen, J. S.: Composition,
793 mixing state, and size distribution of single submicron particles during pollution episodes in a coastal
794 city in southeast China, Environ. Sci. Pollut. Res., 26, 1464–1473,
795 https://doi.org/10.1007/s11356-018-3469-x, 2018.
796 Xu, W. Q., Han, T. T., Du, W., Wang, Q. Q., Chen, C., Zhao, J., Zhang, Y. J., Li, J., Fu, P. Q., Wang, Z. F.,

Worsnop, D. R., and Sun, Y. L.: Effects of aqueous-phase and photochemical processing on secondary organic aerosol formation and evolution in Beijing, China, Environ. Sci. Technol., 51, 762−770, https://doi.org/10.1021/acs.est.6b04498, 2017.

Xue, J., Griffth, S. M., Yu, X., Lau, A.K.H., and Yu, J. Z.: Effect of nitrate and sulfate relative abundance in $PM_{2.5}$ on liquid water content explored through half-hourly observations of inorganic soluble aerosols at a polluted receptor site, Atmos. Environ., 99, 24–31, https://doi.org/10.1016/j.atmosenv.2014.09.049, 2014.

Yang, J., Ma, S. X., Gao, B., Li, X. Y., Zhang, Y. J., Cai, J., Li, M., Yao, L. A., Huang, B., and Zheng, M.: Single particle mass spectral signatures from vehicle exhaust particles and the source apportionment of on-line $PM_{2.5}$ by single particle aerosol mass spectrometry, Sci. Total Environ., 593, 310–318, https://doi.org/10.1016/j.scitotenv.2017.03.099, 2017.

Zauscher, M. D., Wang, Y., Moore, M. J. K., Gaston, C. J., and Prather, K. A.: Air Quality Impact and Physicochemical Aging of Biomass Burning Aerosols during the 2007 San Diego Wildfires, Environ. Sci. Technol., 47, 7633–7643, https://doi.org/10.1021/es4004137, 2013.

Zaveri, R. A., Barnard, J., Easter, R., Riemer, N., and West, M.: Particle-resolved simulation of aerosol size, composition, mixing state, and the associated optical and cloud condensation nuclei activation properties in an evolving urban plume, J. Geophys. Res., 115, D17210, https://doi.org/10.1029/2009JD013616, 2010.

Zhang, G. H., Bi, X. H., Chan, L. Y., Li, L., Wang, X. M., Feng, J. L., Sheng, G. Y., Fu, J. M., Li, M., and Zhou, Z.: Enhanced trimethylamine-containing particles during fog events detected by single particle aerosol mass spectrometry in urban Guangzhou, China, Atmos. Environ., 55, 121–126, https://doi.org/10.1016/j.atmosenv.2012.03.038, 2012.

Zhang, G. H., Han, B. X., Bi, X. H., Dai, S. X., Huang, W., Chen, D. H., Wang, X. M., Sheng, G. Y., Fu, J. M., and Zhou, Z.: Characteristics of individual particles in the atmosphere of Guangzhou by single particle mass spectrometry, Atmos. Res., 153, 286–295, https://doi.org/10.1016/j.atmosres.2014.08.016, 2015.

Zhang, J. K., Luo, B., Zhang, J. Q., Ouyang, F., Song, H. Y., Liu, P. C., Cao, P., Schäfer, K., Wang, S. G., Huang, X. J., and Lin, Y. F.: Analysis of the characteristics of single atmospheric particles in Chengdu using single particle mass spectrometry, Atmos. Environ., 157, 91–100, https://doi.org/10.1016/j.atmosenv.2017.03.012, 2017a.

Zhang, G. H., Lin, Q. H., Peng, L., Yang, Y. X., Fu, Y. Z., Bi, X. H., Li, M., Chen, D. H., Chen, J. X., Cai, Z., Wang, X. M., Peng, P. A., Sheng, G. Y., Zhou, Z.: Insight into the in-cloud formation of oxalate based on in situ measurement by single particle mass spectrometry, Atmos. Chem. Phys., 17 (22), 13891–13901, https://doi.org/10.5194/acp-17-13891-2017, 2017b.

Zhang, G. H., Han, B. X., Bi, X. H., Dai, S. X., Huang, W., Chen, D. H., Wang, X. M., Sheng, G. Y., Fu, J. M., and Zhou, Z.: Characteristics of individual particles in the atmosphere of Guangzhou by single particle mass spectrometry, Atmos. Res., 153, 286–295, https://dx.doi.org/10.1016/j.atmosres.2014.08.016, 2015.

Zhang, G. H., Lian, X. F., Fu, Y. Z., Lin, Q. H., Li, L., Song, W., Wang, Z. Y., Tang, M. J., Chen, D. H., Bi, X. H., Wang, X. M., and Sheng, G. Y.: High secondary formation of nitrogen-containing organics (NOCs) and its possible link to oxidized organics and ammonium, Atmos. Chem. Phys., 20, 1469–1481, https://doi.org/10.5194/acp-20-1469-2020, 2020.

Zhang, X. H., Xu, J. Z., Kang, S. C., Zhang, Q., and Sun, J. Y.: Chemical characterization and sources of submicron aerosols in the northeastern Qinghai–Tibet Plateau: insights from high-resolution mass

spectrometry, Atmos. Chem. Phys., 19, 7897−7911, https://doi.org/10.5194/acp-19-7897-2019, 2019a.
Zhang, G. H., Lin, Q. H., Peng, L., Yang, Y. X., Jiang, F., Liu, F. X., Song, W., Chen, D. H., Cai, Z., Bi, X. H., Miller, M., Tang, M. J., Huang, W. L., Wang, X. M., Peng, P. A., Shen, G. Y.: Oxalate Formation Enhanced by Fe-Containing Particles and Environmental Implications, Environ. Sci. Technol., 53, 1269–1277, https://doi.org/10.1021/acs.est.8b05280, 2019b.
Zhang, N. N., Cao, J. J., Xu, H. M., and Zhu, C. S.: Elemental compositions of $PM_{2.5}$ and TSP in Lijiang, southeastern edge of Tibetan Plateau during pre-monsoon period, Particuology, 11(1), 63–69, https://doi.org/10.1016/j.partic.2012.08.002, 2013.
Zhang, S. P., Xing, J., Sarwar, G., Ge, Y. L., He, H., Duan, F. K., Zhao, Y., He, K. B., Zhu, L. D., Chu, B. W.: Parameterization of heterogeneous reaction of $SO_2$ to sulfate on dust with coexistence of $NH_3$ and $NO_2$ under different humidity conditions, Atmos. Environ., 208, 133–140, https://doi.org/10.1016/j.atmosenv.2019.04.004, 2019c.
Zhao, S. Y., Tie, X. X., Long, X., and Cao, J. J.: Impacts of Himalayas on black carbon over the Tibetan Plateau during summer monsoon, Sci. Total Environ., 598, 307–318, https://doi.org/10.1016/j.scitotenv.2017.04.101, 2017.

Table 1. The number concentrations, average percentages and characteristic ions of nine types of particles during the entire campaign, and the average percentages of the major six particle types during two episodes.

| Type | Number count | Fraction in total (%) | Episode 1 (%) | Episode 2 (%) | Tracer ions |
|---|---|---|---|---|---|
| rich-K | 151040 | 30.9 | 29.0 | 39.3 | $^{39}K^+$, $^{26}CN^-$, $^{42}CNO^-$, $^{46}NO_2^-$, $^{62}NO_3^-$, $^{97}HSO_4^-$ |
| BB | 91322 | 18.7 | 11.5 | 14.2 | $^{39}K^+$, levoglucosan ($^{45}CHO_2^-$, $^{59}C_2H_3O_2^-$, $^{71}C_3H_3O_2^-$, $^{73}C_3HO_3^-$), $^{26}CN^-$, $^{35,37}Cl^-$, $^{42}CNO^-$, $^{46}NO_2^-$, $^{62}NO_3^-$, $^{97}HSO_4^-$ |
| OC | 62446 | 12.8 | 8.1 | 10.0 | $^{27}C_2H_3^+$, $^{37}C_3H^+$, $^{38}C_3H_2^+$, $^{39}K^+/C_3H_3^+$, $^{43}C_2H_3O^+$, $^{51}C_4H_3^+$, $^{26}CN^-$, $^{42}CNO^-$, $^{46}NO_2^-$, $^{62}NO_3^-$, $^{97}HSO_4^-$ |
| Ammonium | 58317 | 11.9 | 17.5 | 13.5 | $^{12}C^+$, $^{18}NH_4^+$, $^{39}K^+$, $^{58}C_2H_5NHCH_2^+$, $^{97}HSO_4^-$, $^{195}H(HSO_4)_2^-$ |
| EC-aged | 53337 | 10.9 | 10.0 | 17.2 | $C_n^{\pm}$ (n =1 ~ 5), $^{39}K^+$, $^{97}HSO_4^-$ |
| Dust | 52533 | 10.7 | 20.3 | 1.3 | $^{40}Ca^+$, $^{56}CaO^+$, $^{16}O^-$, $^{17}OH^-$, $^{76}SiO_3^-$, $^{79}PO_3^-$ |
| NaK-SN | 13726 | 2.8 | na | na | $^{23}Na^+$, $^{39}K^+$, $^{62}NO_3^-$, $^{97}HSO_4^-$ |
| Metal | 4672 | 1.0 | na | na | $^{51}V^+$, $^{56}Fe^+$, $^{64,66,68}Zn^+$, $^{206,207,208}Pb^+$ |
| Others | 1580 | 0.3 | na | na | No obvious characteristic peaks |

**Figure captions:**

**Figure 1.** Box and whisker diurnal plots of the number concentration of the main particle types (a) rich-Potassium (K), (b) Biomass burning (BB), (c) Organic carbon (OC), (d) Ammonium, (e) Element carbon (EC)-aged, (f) Dust in hourly resolution. The lower, middle, and upper lines of the boxes denote the $25^{th}$, $50^{th}$, and $75^{th}$ percentiles. The lower and upper whiskers represent the $10^{th}$ and $90^{th}$ percentiles, respectively. Average values are shown in white dots.

**Figure 2.** Maps of the mean HYSPLIT back trajectory clusters (72 h) at the height of 500 m during the whole field observation. Embedded pie chart represents the relative fraction of each particle type in the four clusters.

**Figure 3.** Size distributions of the relative number fraction (%) of the total particles for nine groups during (a) the total sampling campaign and two episodes of (b) E1 and (c) E2.

**Figure 4.** Number fractions of secondary markers associated with the six particle types (rich-K, BB, OC, Ammonium, EC-aged, Dust) during the whole observation. Secondary species include sulfate ($^{97}HSO_4^-$), sulfuric acid ($^{195}H(HSO_4)_2^-$), nitrate ($^{62}NO_3^-$), ammonium ($^{18}NH_4^+$), amine ($^{58}C_2H_5NHCH_2^+$), and oxalate ($^{89}HC_2O_4^-$) ions.

**Figure 5.** Number fractions of secondary markers associated with the six particle types (i.e., rich-K, BB, OC, Ammonium, EC-aged, and Dust) in four clusters. Secondary species abbreviations as in Figure 4.

**Figure 6.** Correlations between the relative number fractions of the secondary species (a) $^{43}C_2H_3O^+$, (b) $^{89}HC_2O_4^-$, (c) $^{18}NH_4^+$, (d) $^{62}NO_3^-$, (e) $^{97}HSO_4^-$ and $O_x$ concentration during E1 (blue square) and E2 (red dot).

**Figure 7.** Correlations between the relative number fractions of the secondary species (a) $^{43}C_2H_3O^+$, (b) $^{89}HC_2O_4^-$, (c) $^{18}NH_4^+$, (d) $^{62}NO_3^-$, (e) $^{97}HSO_4^-$ and relative humidity (RH) during E1 (cyan dot) and E2 (orange square).

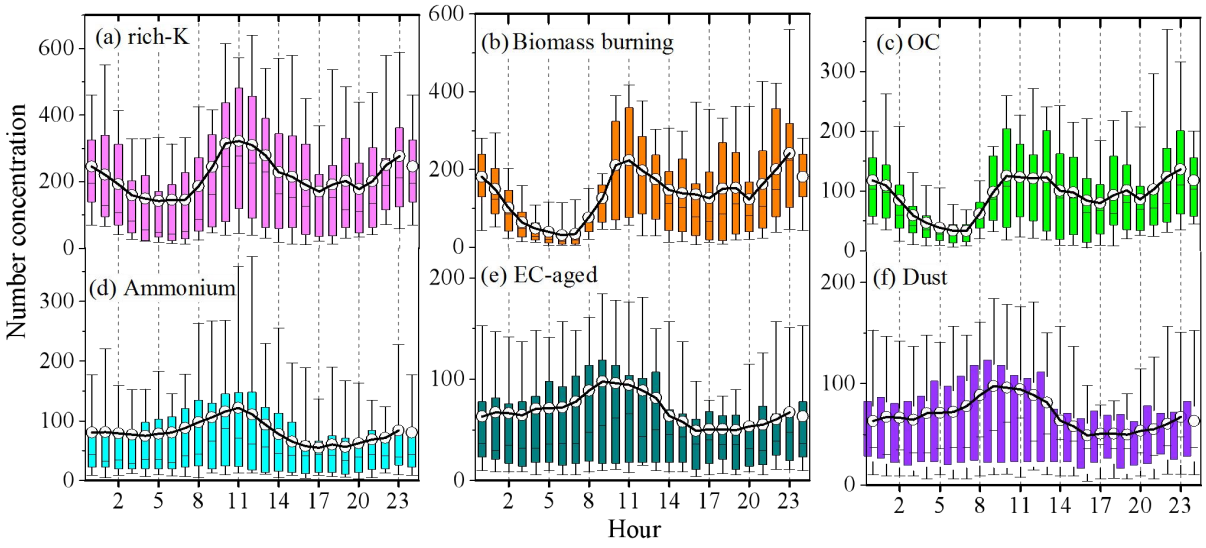


Figure 1. Box and whisker diurnal plots of the number concentration of the main particle types (a) rich-Potassium (K), (b) Biomass burning (BB), (c) Organic carbon (OC), (d) Ammonium, (e) Element carbon (EC)-aged, (f) Dust in hourly resolution. The lower, middle, and upper lines of the boxes denote the 25$^{th}$, 50$^{th}$, and 75$^{th}$ percentiles. The lower and upper whiskers represent the 10$^{th}$ and 90$^{th}$ percentiles, respectively. Average values are shown in white dots.

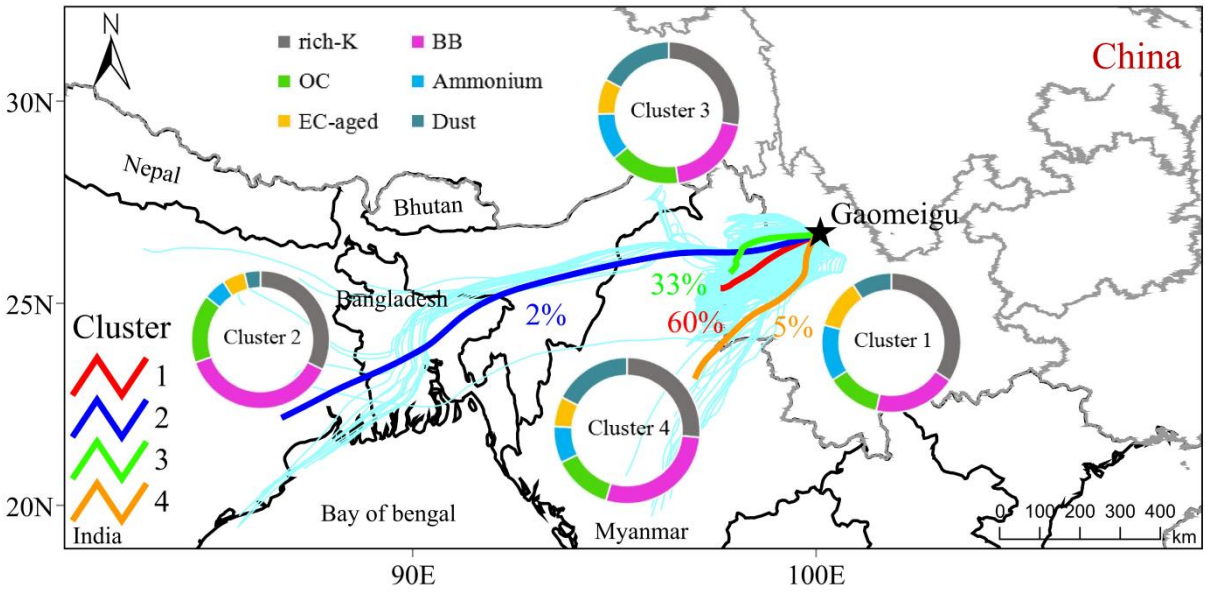


892

893 Figure 2. Maps of the mean HYSPLIT back trajectory clusters (72 h) at the height of 500 m during the
894 whole field observation. Embedded pie chart represents the relative fraction of each particle type in the
895 four clusters.

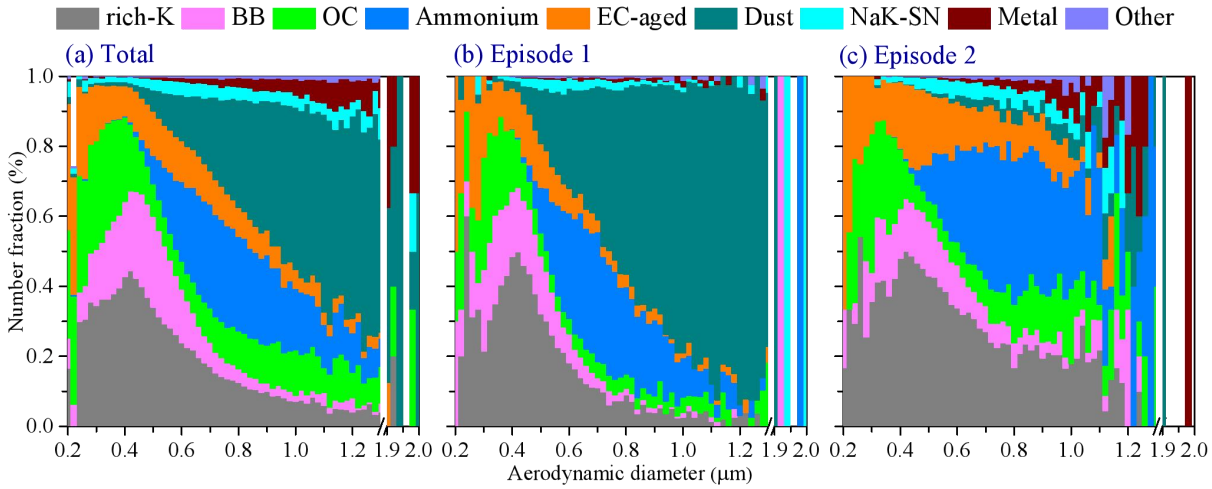


Figure 3. Size distributions of the relative number fraction (%) of the total particles for nine groups during (a) the total sampling campaign and two episodes of (b) E1 and (c) E2.

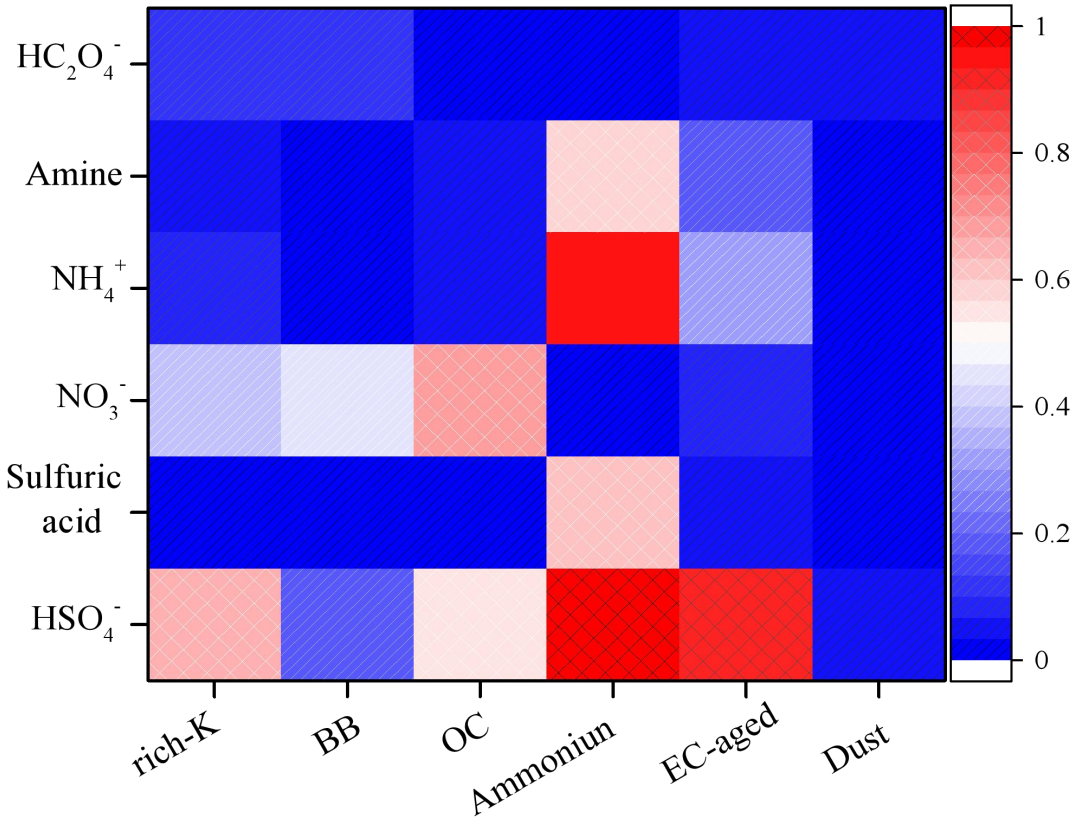


899

900 Figure 4. Number fractions of secondary markers associated with the six particle types (rich-K, BB, OC,
901 Ammonium, EC-aged, Dust) during the whole observation. Secondary species include sulfate ($^{97}HSO_4^-$),
902 sulfuric acid ($^{195}H(HSO_4)_2^-$), nitrate ($^{62}NO_3^-$), ammonium ($^{18}NH_4^+$), amine ($^{58}C_2H_5NHCH_2^+$), and oxalate
903 ($^{89}HC_2O_4^-$) ions.

904

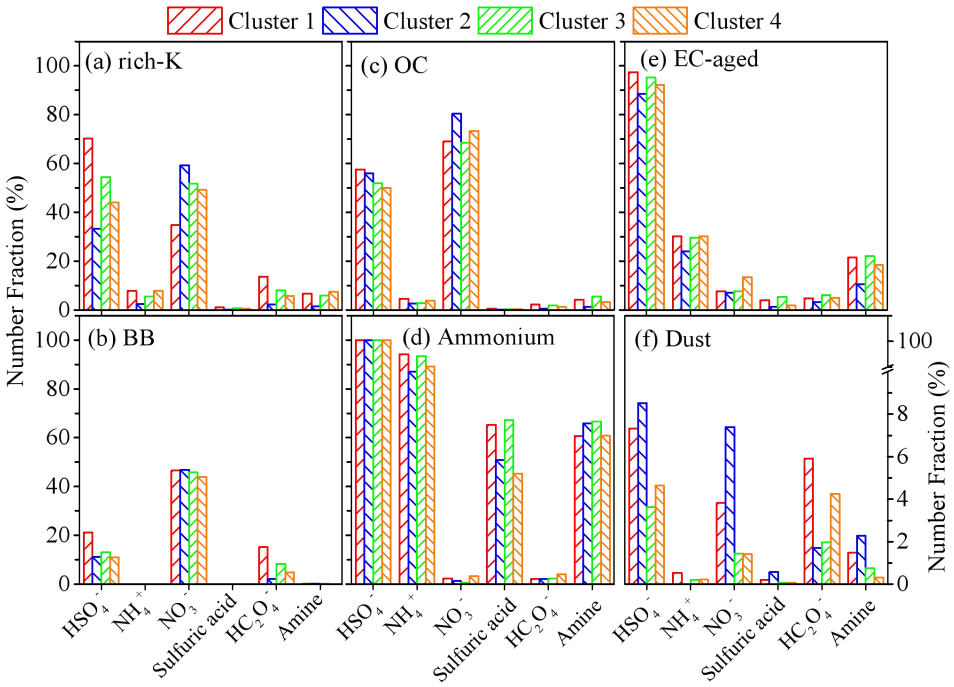


Figure 5. Number fractions of secondary markers associated with the six particle types (i.e., rich-K, BB, OC, Ammonium, EC-aged, and Dust) in four clusters. Secondary species abbreviations as in Figure 4.

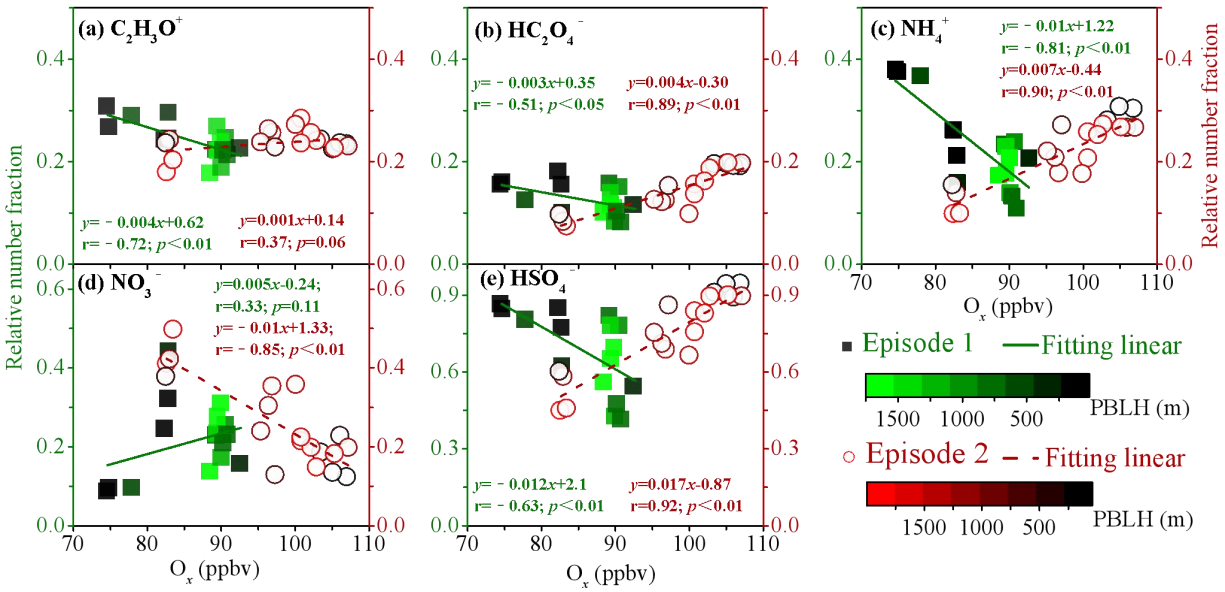


Figure 6. Correlations between the relative number fractions of the secondary species (a) $^{43}C_2H_3O^+$, (b) $^{89}HC_2O_4^-$, (c) $^{18}NH_4^+$, (d) $^{62}NO_3^-$, (e) $^{97}HSO_4^-$ and $O_x$ concentration during E1 (blue square) and E2 (red dot).

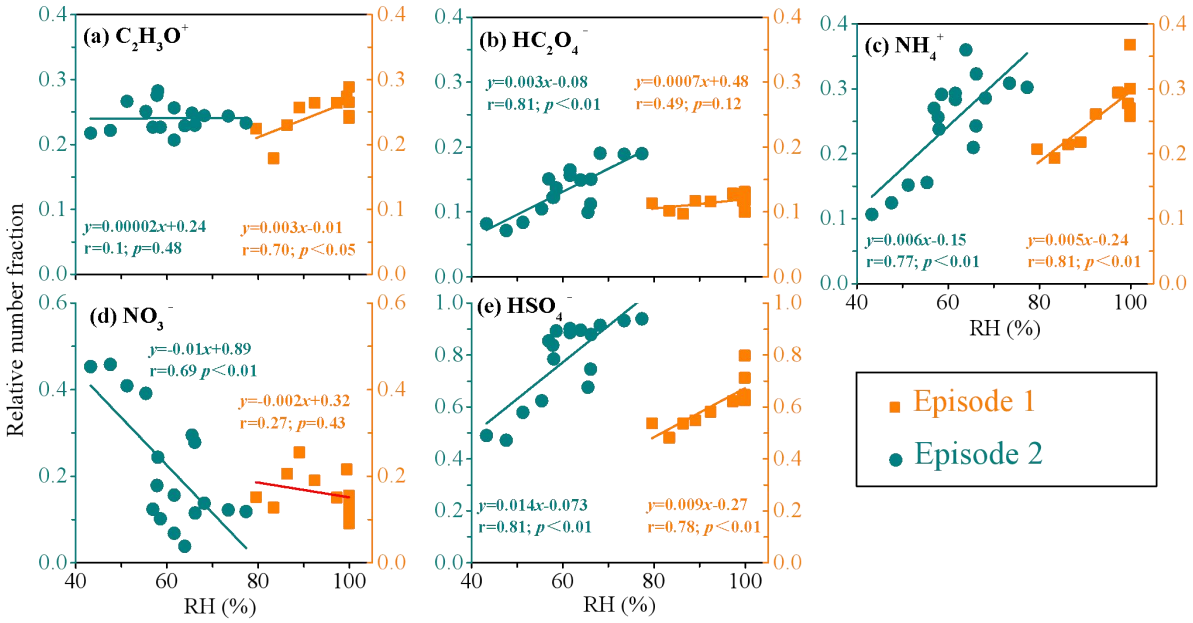


Figure 7. Correlations between the relative number fractions of the secondary species (a) $^{43}C_2H_3O^+$, (b) $^{89}HC_2O_4^-$, (c) $^{18}NH_4^+$, (d) $^{62}NO_3^-$, (e) $^{97}HSO_4^-$ and relative humidity (RH) during E1 (cyan dot) and E2 (orange square).